Signal processing strategies that improve performance and understanding of the quantitative ultrasound SPECTRAL FIT algorithm

Timothy A. Bigelow and William D. O'Brien, Jr.[a)]
Bioacoustics Research Laboratory, Department of Electrical and Computer Engineering, University of Illinois, 405 North Mathews, Urbana, Illinois 61801

(Received 11 August 2004; revised 10 June 2005; accepted 20 June 2005)

Quantifying the size of the tissue microstructure using the backscattered power spectrum has had limited success due to frequency-dependent attenuation along the propagation path, thus masking the frequency dependence of the scatterer size. Previously, the SPECTRAL FIT algorithm was developed to solve for total attenuation and scatterer size simultaneously [Bigelow *et al.*, J. Acoust. Soc. Am. **117**, 1431–1439 (2005)]. Herein, the outcomes from signal processing strategies on the SPECTRAL FIT algorithm are investigated. The signal processing methods can be grouped into two categories, viz., methods that improve the performance of the algorithm and methods that provide insight. The methods that improve the performance include compensating for the windowing function used to gate the time-domain signal, averaging the spectra in the normal frequency domain rather than the log domain to improve the precision of the scatterer size and attenuation estimates, improving the selection of the usable frequency range for the SPECTRAL FIT algorithm, and improving the compensation for electronic noise. The methods that provide insight demonstrate that the anomalous rapid fluctuations of the backscattered power spectrum do not affect the SPECTRAL FIT algorithm, and accurate attenuation estimates can be obtained even when the correct scatterer geometry (i.e., form factor) is not known.
 [DOI: 10.1121/1.2000752]

PACS number(s): 43.80.Ev, 43.80.Qf, 43.80.Vj [FD] Pages: 1808–1819

LIST OF SYMBOLS

a_{eff} = effective radius of scatterer;
$a_{\text{eff}\,j}$ = estimated effective radius of scatterer found from one set (i.e., 25 averaged rf echoes) of simulated backscatter wave forms;
$\bar{a}_{\text{eff}}$ = mean value of estimated effective radius from all sets of backscattered wave forms (i.e., $\bar{a}_{\text{eff}}=\Sigma_{\forall j}a_{\text{eff}\,j}/\Sigma_{\forall j}j$);
ASD = average squared difference term minimized by SPECTRAL FIT algorithm;
c = speed of sound in the tissue;
c_0 = speed of sound in water;
$E[\ ]$ = expected value with respect to scattering random process;
$E_N[\ ]$ = expected value with respect to electronic noise random process;
f = frequency;
f_0 = frequency corresponding to the spectral peak of the Gaussian spectrum, i.e.,

$$\exp\left(-\left(\frac{f-f_0}{\sqrt{2}\sigma_\omega}\right)^2\right);$$

$F_\gamma(f,a_{\text{eff}})$ = form factor related to the scatterer geometry and size;
$f\#$ = f-number for spherically focused transducer;
G_{corr} = windowing correction term for spectrum;
g_{win} = windowing function used to gate the time-domain wave forms;
g_{win2} = windowing function used for homomorphic filtering;
G_{win} = Fourier transform of $g_{\text{win}}(t)$;
$H(f)$ = filtering characteristics of ultrasound source;
k = wave number in tissue;
L = length of the windowing function;
n = frequency exponent when Gaussian form factor is varied [i.e., $F_\gamma(f,a_{\text{eff}})=\exp(-0.827\cdot(ka_{\text{eff}})^n)$];
$N(f)$ = additive electronic noise spectrum;
N_{dB} = minimum value allowed for N_{Floor} when no electronic noise has been added;
N_{Floor} = noise floor of system used when selecting usable frequencies;
$P_n, P_p, \bar{P}_n$ = terms used to fit Gaussian distribution to spectrum in log domain;
P_{ref} = reference spectrum [i.e., $P_{\text{ref}}(f)=k_0^4|V_{\text{inc}}(\omega)|^2|H(\omega)|^4$];
P_{scat} = $E[|V_{\text{refl}}|^2]$ estimated from set of wave forms;
SNR = signal-to-noise ratio;
s_z = integration variable of field along beam axis;
t = time;
T_{cep} = value used to set the amount of homomorphic filtering;
T_{win} = length windowing function applied to time-domain wave form (i.e., $T_{\text{win}}=2L/c$);

[a)]Electronic mail: wdo@uiuc.edu

$V_{\text{cep}i}$ = rf echo expressed in cepstral domain;
V_{inc} = voltage spectrum applied to ultrasound source;
V_j = voltage spectrum produced by a single backscattered rf echo;
v_{noise} = example noise signal voltage in time domain (i.e., no signal transmitted by source);
V_{plane} = voltage spectrum produced by backscatter from rigid plane placed at the focal plane [i.e., proportional to $V_{\text{inc}}(\omega)(H(\omega))^2 e^{i2k_0 z_T}$];
V_{refl} = voltage spectrum produced by backscatter from tissue containing scatterers;
$v_{\text{refl}i}$ = voltage of a rf echo in time domain;
w_x, w_y, w_z = equivalent Gaussian dimensions of velocity potential field in focal region;
$X, \bar{X}$ = terms used in minimization scheme for SPECTRAL FIT algorithm;
z_T = distance from ultrasound source's aperture plane to focal plane;
α = total effective attenuation coefficient for tissue between ultrasound source and region containing the scatterers (i.e., assumed linear frequency dependence of the form $\alpha = \alpha_0 f$);
α_1 = local attenuation coefficient of the tissue in the region containing the scatterers;
α_0 = slope of total attenuation coefficient versus frequency;
$(\alpha_0 z_T)_j$ = estimated attenuation along the propagation path for single data set;
$\overline{(\alpha_0 z_T)}$ = mean value for attenuation along the propagation path from all sets of backscattered wave forms [i.e., $\overline{(\alpha_0 z_T)} = \Sigma_{\forall j}(\alpha_0 z_T)_j / \Sigma_{\forall j} j$];
$\sigma_{a_{\text{lower}}}$ = percent deviation in values of scatterer size for sizes smaller than the mean size (i.e., $a_{\text{eff}\,j} < \bar{a}_{\text{eff}}$);
$\sigma_{a_{\text{upper}}}$ = percent deviation in values of scatterer size for sizes larger than the mean size (i.e., $a_{\text{eff}\,j} > \bar{a}_{\text{eff}}$);
σ_g = bandwidth term for the Gaussian distribution approximating the windowing function (i.e., $|G_{\text{win}}(f)|^2 \propto e^{f^2/2\sigma_g^2}$);
$\sigma_{\alpha_{\text{lower}}}$ = deviation in dB/MHz in values of attenuation for attenuations smaller than the mean attenuation [i.e., $(\alpha_0 z_T)_j < \overline{(\alpha_0 z_T)}$];
$\sigma_{\alpha_{\text{upper}}}$ = deviation in dB/MHz in values of attenuation for attenuations greater than the mean attenuation [i.e., $(\alpha_0 z_T)_j > \overline{(\alpha_0 z_T)}$];
σ_ω = bandwidth term for Gaussian distribution, i.e.,

$$\exp\left(-\left(\frac{f-f_0}{\sqrt{2}\sigma_\omega}\right)^2\right)$$

τ_{cep} = time values in cepstral domain.

I. INTRODUCTION

In recent years, an explosion of new medical imaging technologies has occurred. For each technology, quantitative information is the desired outcome to further assist the clinician in making a diagnosis or monitoring a therapy. One method for obtaining quantitative ultrasound (QUS) information is to use the frequency dependence of the *in vivo* backscattered power spectrum to estimate a characteristic size of the tissue microstructure (Lizzi *et al.*, 1983; 1986; Insana *et al.*, 1990). These scatterer size estimates, and related processing strategies, have shown potential for differentiating tumor types (Oelze *et al.*, 2004) as well as assessing the effects of ultrasound therapy (Lizzi *et al.*, 1997a). Unfortunately, the full diagnostic potential of scatterer size estimates has not been realized due to frequency-dependent attenuation along the propagation path between the transducer and the scattering region (i.e., total attenuation).

Current size estimation algorithms assume that the total attenuation is known *a priori*. Errors in the assumed attenuation result in inaccuracies in the scatterer size estimate of the same magnitude as the errors in the assumed attenuation. Although tissues with drastically different characteristic sizes can be distinguished based on the scatterer size (using an assumed total attenuation), subtle differences, such as assessing the disease state of liver (Lu *et al.*, 1999), will probably be missed. Excellent clinical results have been obtained for ophthalmologic tumors (Lizzi *et al.*, 1983; 1997a; 1997b; Silverman *et al.*, 2003) as well as carotid plaque (Noritomi *et al.*, 1997; Lee *et al.*, 1998) due to the negligible or known total attenuation (i.e., attenuation of water). In general, however, the uncertainties in the total attenuation reduce the applicability of scatter size for clinical applications.

In addition to limiting the applicability of the size estimates, uncertainties in total attenuation also limit other QUS methods. For example, tissue elasticity can be determined by applying a known external force at the skin surface and estimating the resulting internal tissue displacement (Ophir *et al.* 1991; Skovoroda *et al.*, 1994; O'Donnell *et al.*, 1994; Skovoroda *et al.*, 1995). A related technique, acoustic radiation force impulse imaging (ARFI), uses ultrasound to generate the force within the body that then produces the desired tissue displacement (Nightingale *et al.*, 2000; Lizzi *et al.*, 2003). Unfortunately, the force applied using ARFI is currently unknown due to uncertainties in the radiation force, and hence, the elasticity of the tissue cannot be quantified. However, an estimate of the radiation force could potentially be obtained from an estimate of the total attenuation along the propagation path. Therefore, an accurate estimate of the total attenuation might allow ARFI to quantify tissue elasticity as well.

A new method has been proposed to estimate scatterer size and total attenuation simultaneously using an algorithm termed SPECTRAL FIT (SF) (Bigelow *et al.*, 2005). Using that algorithm, accurate estimates of size and attenuation were obtained for different attenuation values and signal-to-noise levels for larger window lengths. Unfortunately, the precision of the estimates was poor limiting the resolution when forming QUS images of tissue. The poor precision meant that a large number of rf echoes were required before reliable estimates could be obtained increasing the size of the resolution cell. The formation of improved QUS images could potentially allow for early detection of tumors, identification

of a tumor type, or other pathology. The goal of the work reported herein is to investigate different signal processing strategies capable of providing more accurate (i.e., lower mean error) and precise (i.e., smaller deviation) estimates of scatterer size and total attenuation. Successful signal processing techniques included averaging of the power spectra in the normal frequency domain rather than the log domain to improve the precision, correcting for the windowing of the time-domain wave forms to improve the accuracy at smaller window lengths, improving the automatic selection of the frequency range used to obtain the estimates, and improving the compensation of electronic system noise to allow more accurate estimates. Other signal processing strategies did not improve the performance of the estimation scheme; however, these methods are included in this paper because they provide insight into the problem that could guide future investigations.

II. METHODS THAT IMPROVED PERFORMANCE

The signal processing methods that improved the performance of the estimation algorithm will be considered first. A brief review of the SF algorithm is provided before discussing the proposed signal processing strategies.

A. Overview of SPECTRAL FIT algorithm

The expected squared voltage produced by the backscatter returned from a region of interest (ROI) that contains randomly positioned weak scatterers is proportional to (Bigelow and O'Brien, 2004)

$$E[|V_{\mathrm{refl}}(f)|^2] \propto f^4 |V_{\mathrm{inc}}(f)|^2 |H(f)|^4 e^{-4\alpha(f) z_T} F_\gamma(f, a_{\mathrm{eff}}) \times \int_{-L/2}^{L/2} ds_z (g_{\mathrm{win}}(s_z) e^{-4 s_z^2 / w_z^2(f)} e^{4\alpha_1(f) s_z}) \quad (1)$$

while the squared voltage produced by the backscatter returned from a rigid plane placed at the focal plane is proportional to (Bigelow and O'Brien, 2004)

$$|V_{\mathrm{plane}}(f)|^2 \propto |V_{\mathrm{inc}}(f)|^2 |H(f)|^4. \quad (2)$$

If the transducer is assumed to be weakly focused (e.g., f/4), the time gate used to window the backscattered rf echoes is relatively small compared to the depth of focus (i.e., local plane wave approximation), the attenuation in the focal region does not significantly alter the spectrum over the length of the window, and the total attenuation has a linear dependence of frequency (i.e., $\alpha = \alpha_0 f$), then the integral in Eq. (1) can be simplified, and the expected squared voltage produced by the backscatter from the tissue's ROI is approximately proportional to

$$E[|V_{\mathrm{refl}}(f)|^2] \propto f^4 |V_{\mathrm{plane}}(f)|^2 e^{-4\alpha_0 z_T f} F_\gamma(f, a_{\mathrm{eff}}). \quad (3)$$

Hence, by comparing the expected voltage from the ROI to the voltage from a rigid plane placed at the focal plane, an estimate for the total attenuation along the propagation path α as well as the scatterer size a_{eff} can be obtained. In the SF algorithm, the comparison is performed by finding the values of α_0 and a_{eff} that minimize the average squared difference (ASD) given by

$$\mathrm{ASD} = \underset{f}{\mathrm{mean}}[(X(f, a_{\mathrm{eff}}, \alpha_0) - X(a_{\mathrm{eff}}, \alpha_0))^2], \quad (4)$$

where

$$X(f, a_{\mathrm{eff}}, \alpha_0) = \ln\left(\frac{P_{\mathrm{scat}}(f)}{\max_f (P_{\mathrm{scat}}(f))} \right) - \ln\left(\frac{P_{\mathrm{ref}}(f) F_\gamma(f, a_{\mathrm{eff}}) e^{-4\alpha_0 f z_T}}{\max_f (P_{\mathrm{ref}}(f) F_\gamma(f, a_{\mathrm{eff}}) e^{-4\alpha_0 f z_T})} \right), \quad (5)$$

$$\bar{X}(a_{\mathrm{eff}}, \alpha_0) = \underset{f}{\mathrm{mean}}[X(f, a_{\mathrm{eff}}, \alpha_0)].$$

P_{scat} is an estimate of $E[|V_{\mathrm{refl}}(f)|^2]$ obtained from a set of backscattered wave forms, and P_{ref} is given by

$$P_{\mathrm{ref}}(f) = k_0^4 |V_{\mathrm{plane}}(\omega)|^2. \quad (6)$$

Subtracting by $\bar{X}(a_{\mathrm{eff}}, \alpha_0)$ removes the effects of multiplicative constants.

B. Verifying calculation of P_{scat}

When using the SF algorithm, the first requirement is to obtain a good approximation of $E[|V_{\mathrm{refl}}(f)|^2]$ (i.e., P_{scat}) from a set of backscattered wave forms. In our earlier paper (Bigelow *et al.*, 2005) P_{scat} was calculated by averaging the spectra of 25 rf echoes in the log domain, that is,

$$P_{\mathrm{scat}}(f) = \exp\left(\frac{1}{25} \sum_{j=1}^{25} \ln(|V_j(f)|^2) \right). \quad (7)$$

The averaging was performed in the log domain because it was assumed that the transmitted pulse is convolved with the impedance properties of the random medium to generate the reflected rf echo. However, traditionally P_{scat} has been calculated by averaging the wave forms in the normal frequency domain (Insana *et al.*, 1990), that is,

$$P_{\mathrm{scat}}(f) = \frac{1}{25} \sum_{j=1}^{25} |V_j(f)|^2. \quad (8)$$

Therefore, the first signal processing analysis involved determining which method [i.e., Eq. (7) or (8)] yields better performance for the SF algorithm.

The comparison was performed using simulated rf echoes from an infinite half-space placed flush against the aperture plane of a spherically focused f/4 transducer with a focal length of 5 cm. The transducer was excited by an impulse function [i.e., $V_{\mathrm{inc}}(f) = 1$] that had filtering characteristics given by

$$H(f) = \frac{|f| \exp\left(-\left(\frac{f - 8\ \mathrm{MHz}}{6\ \mathrm{MHz}} \right)^2 \right)}{\max_{\forall f}\left(|f| \exp\left(-\left(\frac{f - 8\ \mathrm{MHz}}{6\ \mathrm{MHz}} \right)^2 \right) \right)}. \quad (9)$$

The half-space had an attenuation of 0.3 dB/cm MHz and contained randomly positioned scatterers with Gaussian impedance distributions (i.e., Gaussian scatterers) with effective radii of 25 μm at a density of 35/mm^3. The veloc-

ity potential field from the source was approximated as a three-dimensional Gaussian distribution in the focal region (Bigelow and O'Brien, 2004) where the equivalent Gaussian dimensions were given by

$$w_x = w_y = 0.87\lambda f\#\,,$$
$$w_z = 6.01\lambda(f\#)^2. \tag{10}$$

In the simulations, 1000 rf echoes were generated corresponding to 1000 independent scatterer distributions. Each echo was sampled at a sampling rate of 53 MHz when "digitizing" the signal. The 1000 echoes were then grouped into sets of 25 wave forms so that 40 independent estimates of scatterer size and total attenuation could be obtained. For each rf echo, the wave form was windowed in the time domain using a Hamming windowing function where the length of the time gate was calculated from $T_{\text{win}}=2L/c$. The same length Hamming window (i.e., $T_{\text{win}}=2L/c_0$) was also used to window the signal returned from the rigid plate placed at the focus when obtaining the reference spectrum. The ASD from Eq. (4) was minimized over the set of all frequencies corresponding to signal values satisfying

$$\left\{10\log\left(\frac{P_{\text{scat}}(f)}{\max_{\forall f}(P_{\text{scat}}(f))}\right)\right\}_{\substack{\text{polynomial}\\ \text{fit}}} > \max\left(\left[-30\ \text{mean}\left(\left\{10\log\left(\frac{P_{\text{scat}}(f)}{\max_{\forall f}(P_{\text{scat}}(f))}\right)\right\}_{\substack{\text{polynomial}\\ \text{fit}}}\right)\right]\right), \tag{11}$$

where the spectrum was fit by a polynomial of large degree (i.e., 50) to reduce the impact of spectral variations on the selected frequency range.

The accuracy (error in mean value) and precision (estimate deviation) of the size and total attenuation estimates for calculating P_{scat} according to Eqs. (7) and (8) are shown in Fig. 1. In these plots, the errors in the mean value (i.e., plots I) were the errors between the mean value of all 40 estimates and the true value. The deviations (i.e., plots II) were found by adding the standard deviation values of estimates above and below the mean value. The standard deviations were given by

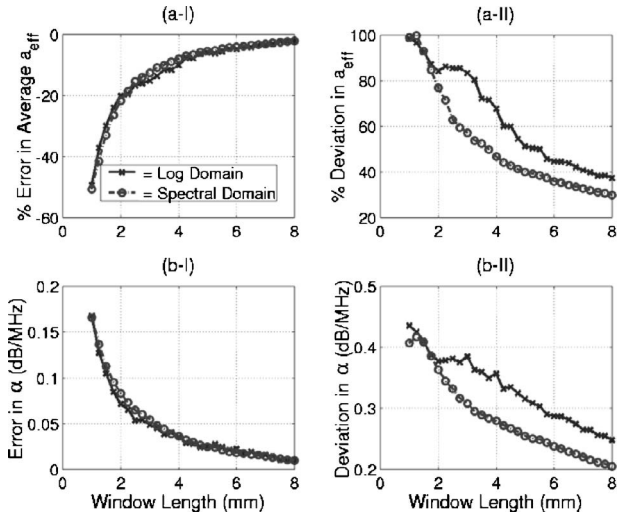

FIG. 1. A comparison between averaging in the normal spectral domain and the log spectral domain to reduce spectral noise due to random scatterer spacing for a half-space with an attenuation of 0.3 dB/cm MHz in the absence of electronic noise: (a) compares the scatterer size estimates and (b) compares the total attenuation estimates. (I) The errors in the mean value for the estimates and (II) the total deviation about the mean estimated values.

$$\sigma_{a_{\text{upper}}} = \frac{100}{a_{\text{eff}}|_{\text{Theory}}}\sqrt{\frac{\sum_{\forall a_{\text{eff}\,j}>\bar{a}_{\text{eff}}}(a_{\text{eff}\,j}-\bar{a}_{\text{eff}})^2}{\sum_{\forall a_{\text{eff}\,j}>\bar{a}_{\text{eff}}} j}},$$
$$\sigma_{a_{\text{lower}}} = \frac{100}{a_{\text{eff}}|_{\text{Theory}}}\sqrt{\frac{\sum_{\forall a_{\text{eff}\,j}<\bar{a}_{\text{eff}}}(a_{\text{eff}\,j}-\bar{a}_{\text{eff}})^2}{\sum_{\forall a_{\text{eff}\,j}<\bar{a}_{\text{eff}}} j}} \tag{12}$$

for the deviation in a_{eff} and

$$\sigma_{\alpha_{\text{upper}}} = \sqrt{\frac{\sum_{\forall(\alpha_0 z_T)_j>\overline{(\alpha_0 z_T)}}((\alpha_0 z_T)_j-\overline{(\alpha_0 z_T)})^2}{\sum_{\forall(\alpha_0 z_T)_j>\overline{(\alpha_0 z_T)}} j}},$$
$$\sigma_{\alpha_{\text{lower}}} = \sqrt{\frac{\sum_{\forall(\alpha_0 z_T)_j<\overline{(\alpha_0 z_T)}}((\alpha_0 z_T)_j-\overline{(\alpha_0 z_T)})^2}{\sum_{\forall(\alpha_0 z_T)_j<\overline{(\alpha_0 z_T)}} j}} \tag{13}$$

for the deviation in total attenuation. The deviations were given by $(\sigma_{\alpha_{\text{upper}}}+\sigma_{\alpha_{\text{lower}}})$ and $(\sigma_{\alpha_{\text{upper}}}+\sigma_{\alpha_{\text{lower}}})$. The mean values of the estimates using Eqs. (7) and (8) are almost identical, but the deviations in the estimates are slightly larger when averaging in the log-domain [i.e., Eq. (7)]. Hence, the precision of the SF algorithm is improved when the spectra from the rf echoes are averaged in the normal frequency domain [i.e., Eq. (8)] rather than in the log domain [i.e., Eq. (7)].

C. Windowing function compensation

In Fig. 1, the accuracy of the estimates from the SF algorithm degrades quickly for window lengths less than 4 mm due to the convolution effects of the windowing function (i.e., windowing in the time domain translates to convolution in the frequency domain) (Akita and Ueda, 1988). This is restrictive because the convolution effects limit the resolution of the QUS image. Hence, the next signal process-

ing strategy endeavored to compensate for the effects of windowing so that smaller windowing functions could be used. One possibility would be to use a reference phantom instead of a rigid plane at the focus to obtain the reference spectrum (Gerig *et al.*, 2003) and then use the same Hamming window on both. However, a reference phantom increases the uncertainty of the estimation technique (Gerig *et al.*, 2003). Furthermore, performing a comprehensive evaluation of the reference phantom technique is difficult because of the need to test materials with attenuation, scatterer type, and scatterer sizes differing from the reference phantom. Hence, the reference phantom technique was not evaluated at this time. Instead, an attempt was made to compensate directly for the windowing effects on the backscattered wave forms while still using a plane placed at the focus as a reference.

It has been shown that windowing of the signals in the time domain is equivalent to a convolution of the power spectra given by (Wear, 2002)

$$E[|V_{\text{refl}}|^2]_{\text{windowed}} \propto E[|V_{\text{refl}}|^2]_{\text{ideal}} * |G_{\text{win}}(f)|^2, \tag{14}$$

where $G_{\text{win}}(f)$ is the Fourier transform of the windowing function. Also, if the windowing function and expected backscattered spectra can be reasonably described by Gaussian distributions given by

$$\begin{aligned} E[|V_{\text{refl}}|^2]_{\text{ideal}} &\propto e^{-(f-f_0)^2/2\sigma_\omega^2}, \\ |G_{\text{win}}(f)|^2 &\propto e^{-f^2/2\sigma_g^2}, \end{aligned} \tag{15}$$

then the windowed backscattered spectrum is approximately given by (Wear, 2002)

$$E[|V_{\text{refl}}|^2]_{\text{windowed}} \propto e^{-(f-f_0)^2/2(\sigma_\omega^2+\sigma_g^2)}. \tag{16}$$

Windowing increases the bandwidth of the backscattered wave form. In Bigelow *et al.* (2005), the scatterer size was related qualitatively to a decrease in the backscattered bandwidth. Hence, the increase in the bandwidth due to windowing is responsible for the underestimate of the scatterer size as was observed in Figs. 1 and 2. Furthermore, the bandwidth broadening, as described in this manner, can be compensated by multiplying the windowed spectrum by

$$G_{\text{corr}} = e^{-(f-f_0)^2\sigma_g^2/2(\sigma_\omega^2+\sigma_g^2)\sigma_\omega^2}. \tag{17}$$

This correction for windowing was also tested using the rf echoes from the half-space described previously. The backscattered spectra from 25 independent rf echoes windowed with Hamming windows without additive electronic noise were averaged in the normal frequency domain [i.e., Eq. (8)] yielding an estimate $E[|V_{\text{refl}}|^2]_{\text{windowed}}$. The resulting average spectrum was then fit by a Gaussian distribution in the log domain, that is,

$$\begin{aligned} &[f_0,(\sigma_\omega^2+\sigma_g^2)] \\ &\quad = \min_{\substack{\forall f_0 \\ \forall(\sigma_\omega^2+\sigma_g^2)}} \{\text{mean}((P_n(f) - P_p(f,f_0,(\sigma_\omega^2+\sigma_g^2)) - \bar{P}_n)^2)\}, \end{aligned} \tag{18}$$

where

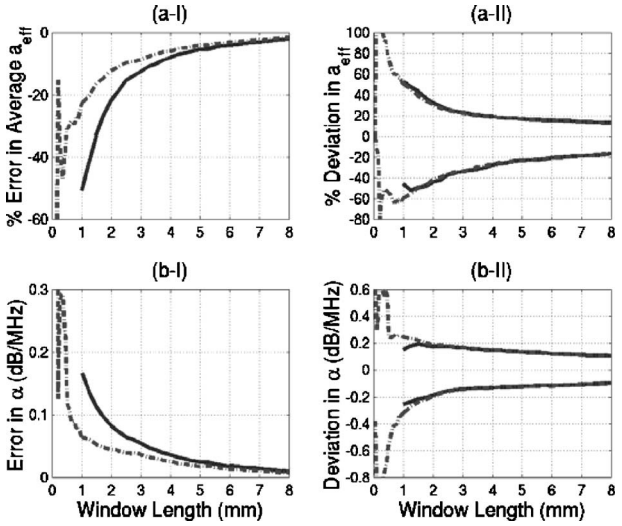

FIG. 2. A comparison between (I) the mean values for the estimates (accuracy) and (II) the deviations about the mean values (precision) for (a) scatterer size and (b) total attenuation when using the same Hamming window to window the reference and backscattered wave forms, (—), and using G_{corr} to correct for the effects of windowing, (-·-). In the simulations, the half-space had an attenuation of 0.3 dB/cm MHz and no electronic noise was added to the backscattered wave forms.

$$\begin{aligned} P_n(f) &= \ln\left(\frac{P_{\text{scat}}(f)}{\max_{\forall f}(P_{\text{scat}}(f))}\right), \\ P_p(f,f_0,(\sigma_\omega^2+\sigma_g^2)) &= -\frac{(f-f_0)^2}{2(\sigma_\omega^2+\sigma_g^2)}, \\ \bar{P}_n &= \text{mean}(P_n(f) - P_p(f,f_0,(\sigma_\omega^2+\sigma_g^2))), \end{aligned} \tag{19}$$

to obtain values for f_0 and $(\sigma_\omega^2+\sigma_g^2)$. The Fourier transform of the Hamming window was also calculated and fit by a Gaussian distribution in the normal frequency domain to obtain the value of σ_g^2. G_{corr} was then calculated and applied from these parameters. Because the effects of windowing on the backscattered spectrum were directly compensated, no windowing was applied to the reference spectrum from the rigid plane. The results of this simulation are shown in Fig. 2 with the results using a Hamming window for both the reference and backscattered signals from Fig. 1. The correction term allows for more accurate estimates of total attenuation and scatterer size (i.e., better than 20%) down to window lengths of 1 mm. However, the precision of the estimates continues to degrade for the smaller window lengths. The loss of precision at smaller window lengths probably results from a reduction in the number of independent samples in the least-squares fit in Eq. (4) due to a loss in the frequency resolution of the spectrum (Wear, 2001).

In this section, a new windowing compensation method was developed and applied to the SF algorithm. Other researchers have developed methods for windowing function compensation for the traditional estimation algorithm where the attenuation was known *a priori* (Akita and Ueda, 1988). Because their work assumed that the total attenuation was known, the performance of the different windowing compensation methods cannot be compared in this study.

D. Improving selection of frequency range

In the earlier simulations, the frequency range used by the SF algorithm was dictated by Eq. (11). However, this definition of the frequency range is not robust and depends significantly on the sampling rate used to acquire the data. Therefore, before the SF algorithm can be reliably implemented, a better definition of the usable frequency range needs to be obtained. Because the principal purpose in selecting the frequency range is to exclude spectral regions dominated by system noise, a suitable alternative would be to select only those frequencies whose signal levels were reasonably larger than the noise floor. Hence, a more generalized selection criteria is given by the set of all frequencies corresponding to signal levels greater than

$$N_{\text{Floor}} = \max\left(\left[N_{\text{dB}}\ \text{mean}\left(10\log\left(\frac{P_{\text{scat}}(f_{N-200}:f_N)}{\max_{\forall f}(\{P_{\text{scat}}(f)\}_{\substack{\text{Gaussian}\\\text{fit}}})}\right)\right)+6\right]\right), \tag{20}$$

where N_{dB} sets a limit on the frequency range in the absence of any electronic noise and f_N refers to the largest positive frequency after taking the Discrete Fourier Transform (DFT) of the sampled wave forms. Also, the signal must be sufficiently oversampled so that at least the last 200 frequency samples would correspond to the additive white electronic system noise. The selection of the last 200 samples, rather than another large number of frequency samples (i.e., last 100 samples), is arbitrary. Six decibels were added to the average of the last 200 samples to ensure that N_{Floor} was always greater than the noise. Smaller values (i.e., 3 dB) were attempted but some of the fluctuations of the noise about its mean value influenced the estimates. A value other than 6 dB may be used on a case-by-case basis by analyzing the deviation of the noise in the last 200 frequency samples, but this possibility is beyond the scope of our current investigation. Furthermore, estimating the noise floor from the last 200 samples is only valid when the noise is white. When the noise is not white, then the noise floor over the relevant frequency range should be estimated from a sample noise signal obtained in the absence of a transmitted signal as was discussed in Bigelow *et al.* (2005).

E. Noise compensation revisited

In another paper (Bigelow *et al.*, 2005), a method to compensate for the additive electronic system noise was introduced. The addition of electronic noise artificially broadened and also reduced (i.e., cannot use information at frequencies below the noise floor) the usable spectrum. Previously, the compensation involved dividing the received spectrum by the term $(1+E_N[|N(f)|^2]/P_{\text{scat}}(f))$ where $E_N[|N(f)|^2]$ was estimated from a reference noise signal in the absence of a transmitted signal in order to eliminate the artificial broadening. However, this compensation method was originally derived when the spectra of the rf echoes were averaged in the log domain rather than the normal frequency domain (i.e., see Sec. II B). Therefore, we need to assure that the same noise compensation is still valid when averaging the spectra in the normal frequency domain. The value of P_{scat} in the presence of electronic noise when averaging in the normal frequency domain is given by

$$\begin{aligned} P_{\text{scat}}(f) &= \frac{1}{25}\sum_{i=1}^{25}\left(|V_i(f)|^2\left(1+\frac{E_N[|N(f)|^2]}{|V_i(f)|^2}\right)\right) \\ &= P_{\text{scat}}(f)_{\text{ideal}}\left(1+\frac{E_N[|N(f)|^2]}{P_{\text{scat}}(f)_{\text{ideal}}}\right). \end{aligned} \tag{21}$$

The artificial broadening is still given by $(1+E_N[|N(f)|^2]/P_{\text{scat}}(f)_{\text{ideal}})$, and dividing the measured P_{scat} by $(1+E_N[|N(f)|^2]/P_{\text{scat}}(f))$ should still reduce the impact of the electronic noise by eliminating the artificial broadening.

Also, $E_N[|N(f)|^2]$ used in compensating for the electronic noise might be obtainable from $P_{\text{scat}}(f_{N-200}:f_N)$, if the spectrum is sufficiently oversampled and the noise is white, removing the need to record the noise in the absence of a transmitted signal. To test this possibility, computer simulations were performed using the same f/4 transducer described when evaluating the calculation of P_{scat} previously in this paper. The half-space for these simulations had an attenuation of 0.05 dB/cm MHz, similar to the half-space used to evaluate the electronic noise compensation by Bigelow *et al.* (2005), and contained randomly positioned Gaussian scatterers with effective radii of 25 μm at a density of 35/mm^3. The rf echoes from 1000 independent scatterer distributions were generated and grouped into 40 sets of 25 wave forms per set for processing. After generating the rf echoes, three different levels of electronic noise were added to the wave forms corresponding to average SNRs of 9, 23, and 36 dB. The SNR values were calculated from

$$\text{SNR} = \frac{1}{25}\sum_{j=1}^{25}\left(10\cdot\log\left(\frac{\int(g_{\text{win}}(t)v_{\text{refl}_j}(t))^2dt}{\int(g_{\text{win}}(t)v_{\text{noise}}(t))^2dt}\right)\right), \tag{22}$$

where v_{refl_j} are the rf echoes from each group of 25 used in the estimate before the noise was added, and v_{noise} is the noise signal used to obtain the estimate for $E_N[|N(f)|^2]$ as described by Bigelow *et al.* (2005). The noise added to each wave form was randomly generated for that wave

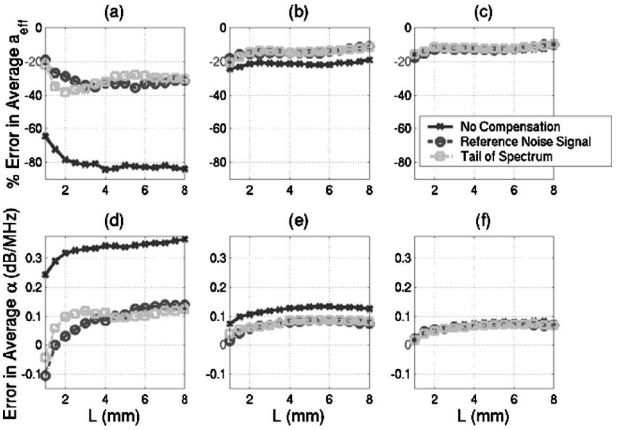

FIG. 3. Comparison of errors in scatterer size estimates for SNRs of (a) 9 dB, (b) 23 dB, and (c) 36 dB as well as attenuation estimates for SNRs of (d) 9 dB, (e) 23 dB, and (f) 36 dB without noise compensation and with different methods for estimating $E_N[|N(f)|^2]$ for a half-space with an attenuation of 0.05 dB/cm MHz.

form while the noise power was set relative to the reference signal from the rigid plane placed at the focal plane. As a result, the SNR for each wave form was slightly different. Hence, Eq. (22) gives the average SNR for the 25 wave forms in a set. The generated noise was zero-mean white with a Gaussian probability density function. The wave forms were analyzed and P_{scat} was compensated for noise using $E_N[|N(f)|^2]$ obtained from both a reference noise signal as well as by averaging the last 200 values of P_{scat}. The convolution effects of windowing were compensated and the frequency range used in the minimization was given by Eq. (20) with N_{dB} set to −20 dB.

The results for both methods of obtaining $E_N[|N(f)|^2]$ are shown in Fig. 3 along with the results obtained without electronic noise compensation. Both methods for obtaining an estimate for $E_N[|N(f)|^2]$ perform about the same and give significant improvement in the accuracy compared to when the electronic noise is not compensated. Due to the comparable performance, in the future $E_N[|N(f)|^2]$ will be found from the last 200 values of P_{scat}, removing the need to record the noise in the absence of a transmitted signal when the noise is white.

III. METHODS THAT PROVIDED INSIGHT

In addition to the signal processing strategies that improved the performance of the SF algorithm, different approaches were attempted that provided no improvement (Bigelow, 2004). Two of the failed approaches are included herein because although they did not work, they provided useful information.

A. Homomorphic deconvolution

One of the signal processing strategies investigated used homomorphic deconvolution (Proakis and Manolakis, 1996) to smooth the backscattered spectrum and hopefully to compensate for the effect of random scatterer spacing thereby improving the precision of the estimates. Each of the backscattered wave forms was gated using a Hamming window $g_{\text{win}}(t)$, converted to the frequency domain, and then filtered according to

$$|V_i|^2 = |\exp(\text{Re}(\text{IFFT}\{V_{\text{cep}i}(\tau_{\text{cep}}) \cdot g_{\text{win2}}(\tau_{\text{cep}})\}))|^2, \tag{23}$$

where

$$V_{\text{cep}i}(\tau_{\text{cep}}) = \text{FFT}\{\ln(|\text{IFFT}\{v_{\text{refl}i}(t) \cdot g_{\text{win}}(t)\}|)\} \tag{24}$$

and

$$g_{\text{win2}} = \begin{cases} 1 & |\tau_{\text{cep}}| \leqslant T_{\text{cep}} \\ 0 & |\tau_{\text{cep}}| > T_{\text{cep}}. \end{cases} \tag{25}$$

The filtered wave forms were then averaged in the normal spectral domain according to Eq. (8), and the effect of convolution due to the Hamming window was compensated.

To test the SF algorithm, simulations were performed using the spherically focused f/4 transducer placed adjacent to an infinite half-space as described previously. This time, 2000 random scatterer distributions were generated. The wave forms from each distribution were then initially grouped in sets of 40 to yield 50 independent estimates of scatterer size and total attenuation for each Hamming window length (varied from 1 to 8 mm). The wave forms were initially taken in sets of 40 instead of 25 to attempt to further improve the precision. (The relationship between varying the number of wave forms in each set and precision will be discussed later in this section.) In addition, a sampling rate of 160 MHz was used when "digitizing" the signal so that the features of the wave forms could be observed better in the cepstral domain. The attenuation of the half-space region was 0.3 dB/cm MHz. The range of frequencies used by the minimization was selected based on Eq. (20) with N_{dB} set to −20 dB.

In the simulations, the value of T_{cep} used to set the amount of filtering was varied as 0.15, 0.31, 0.46, and 0.62 μs. The locations of all of these cutoffs relative to the main spectral peak are shown with an example signal plotted in the cepstral domain in Fig. 4 along with the original unfiltered spectrum. After applying the filter in the cepstral domain, the example spectra were significantly smoothed (Fig. 5). The smaller the value of T_{cep}, the greater the filtering, and the smoother the resulting spectra. The simulation results for the four different filter lengths are shown in Fig. 6. For a filter length of 0.15 μs, the accuracy of the scatterer size estimates was seriously degraded, especially for small window lengths. Hence, the 0.15 μs filter length will not be considered in our detailed analysis of the accuracy and precision given in Fig. 7. In addition to simulating each of the four filtered cases, the simulation was also run without filtering (i.e., $T_{\text{cep}}=\infty$). Hence, the performance of the filtered cases could be compared with the performance available from the unfiltered SF algorithm with 40 wave forms in each set averaged in the normal spectral domain while compensating for the convolution effects of windowing.

In Fig. 7, the accuracy and precision for filter lengths of 0.31, 0.46, and 0.62 μs are compared to the results obtained with no filtering. The accuracy comparison is done by dividing the mean value of the percent error in the scatterer size estimate with filtering by the mean value of the percent error

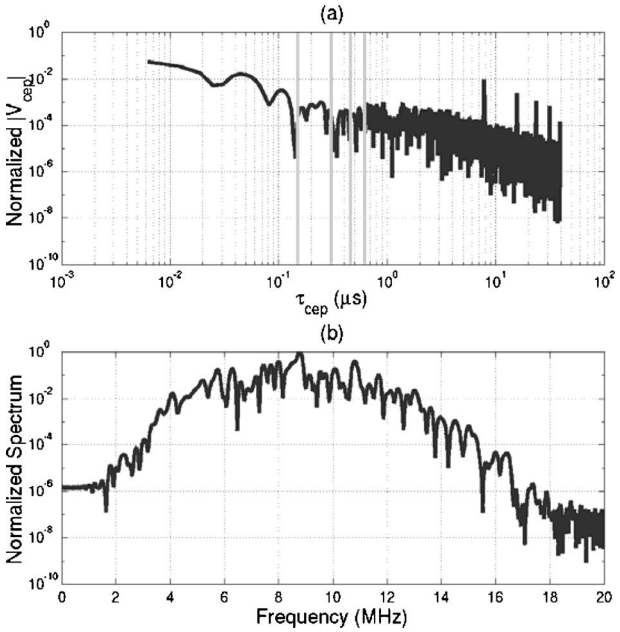

FIG. 4. (a) Example of a spectrum for a single rf echo in cepstral domain showing locations of T_{cep} cutoffs (vertical gray lines) used in the homomorphic deconvolution with (b) the corresponding normalized spectra before any homomorphic processing has been applied.

in the scatterer size estimate without filtering [Fig. 7(a)]. Likewise, the precision comparison is done by dividing the upper [Fig. 7(b)] and lower [Fig. 7(c)] σ values as given by Eq. (12) with filtering by the corresponding values without filtering. An improvement in accuracy or precision would be indicated by a ratio less than one, and degradation in accuracy or precision would be indicated by a ratio greater than one.

From Figs. 6 and 7, the accuracy of the scatterer size estimates is degraded by small filter lengths (0.15 and 0.31 μs). The loss in accuracy at smaller filter lengths is probably due to relevant spectral information being ignored (smoothed out) as a result of the filtering. This is similar to

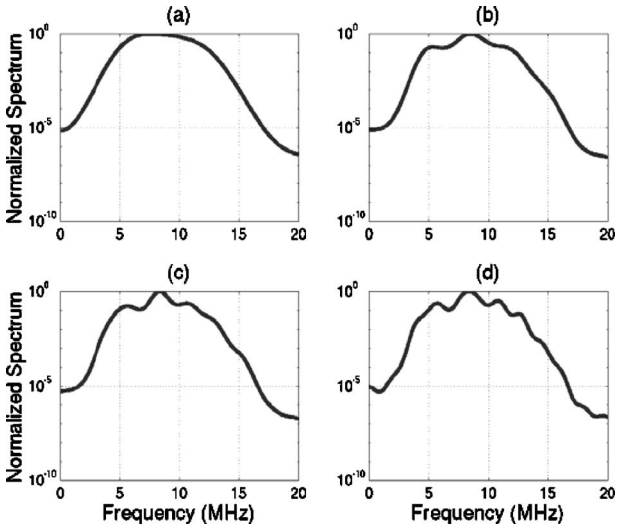

FIG. 5. Example of a normalized spectrum for a single rf echo after applying homomorphic deconvolution with (a) T_{cep}=0.15 μs, (b) T_{cep}=0.31 μs, (c) T_{cep}=0.46 μs, and (d) T_{cep}=0.62 μs.

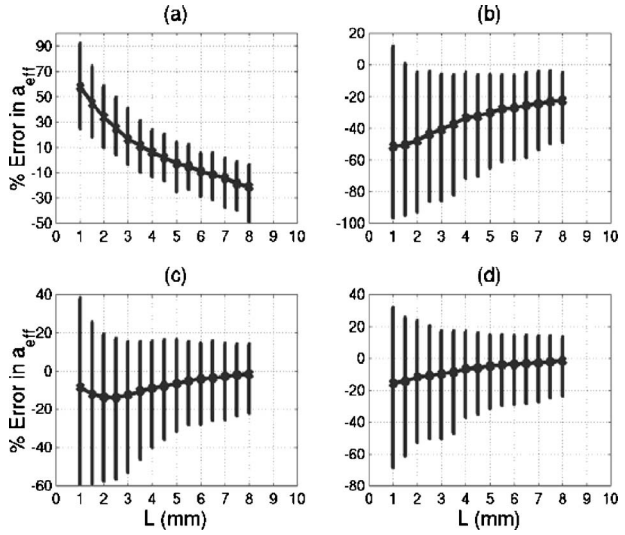

FIG. 6. Percent error in scatterer size estimate for different window lengths after homomorphic deconvolution with (a) T_{cep}=0.15 μs, (b) T_{cep}=0.31 μs, (c) T_{cep}=0.46 μs, and (d) T_{cep}=0.62 μs.

the poor accuracy that was observed when spectral information was ignored by fitting the spectrum to a Gaussian distribution (Bigelow *et al.*, 2005). At larger filter lengths, the accuracy of the scatterer size estimates is slightly improved, especially at larger window lengths [Fig. 7(a)]. In terms of

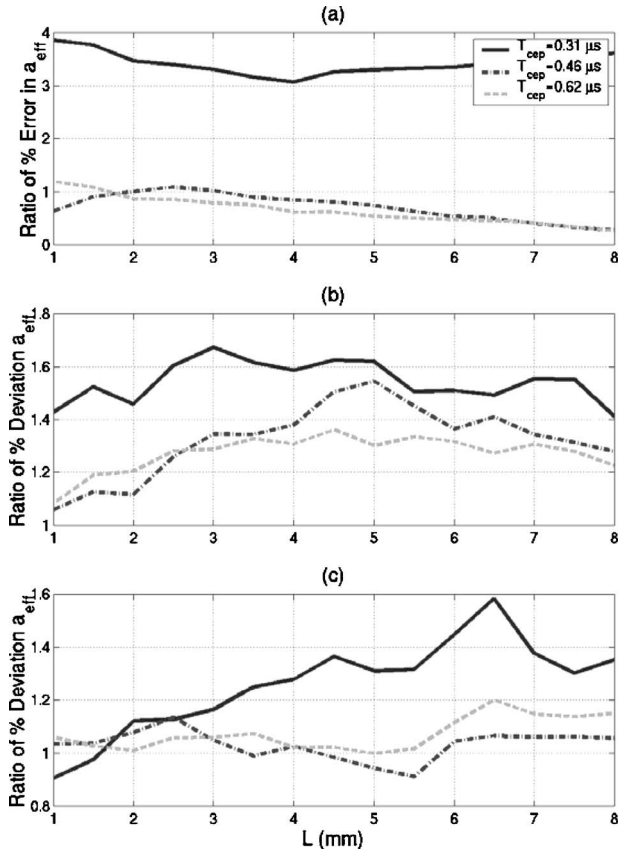

FIG. 7. Simulation results comparing the performance of different homomorphic filter lengths to the performance of the basic SPECTRAL FIT algorithm by plotting (a) the ratio of the average percentage error of the filtered and unfiltered results, (b) the ratio of $\sigma_{a_{upper}}$ of the filtered and unfiltered results, and (c) the ratio of $\sigma_{a_{lower}}$ of the filtered and unfiltered results.

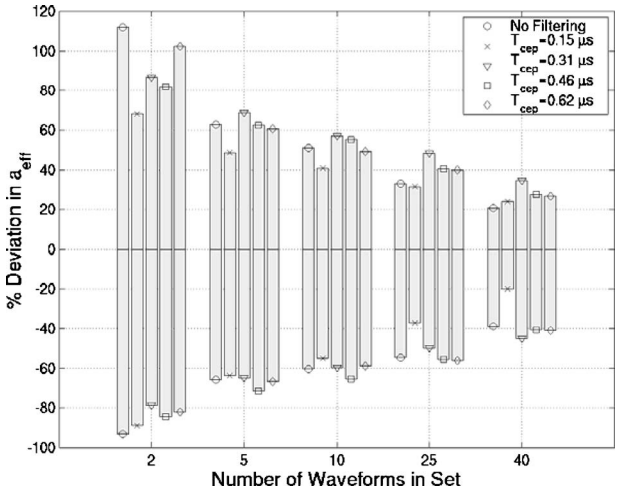

FIG. 8. $\sigma_{a_{\text{upper}}}$ and $\sigma_{a_{\text{lower}}}$ values when a different number of wave forms are averaged in each set before performing the estimate for the different homomorphic deconvolution parameters. The first bar in each group corresponds to the case where no homomorphic filtering was applied to the wave forms while the second, third, fourth, and fifth bars correspond to results for filter lengths of 0.15, 0.31, 0.46, and 0.62 μs, respectively.

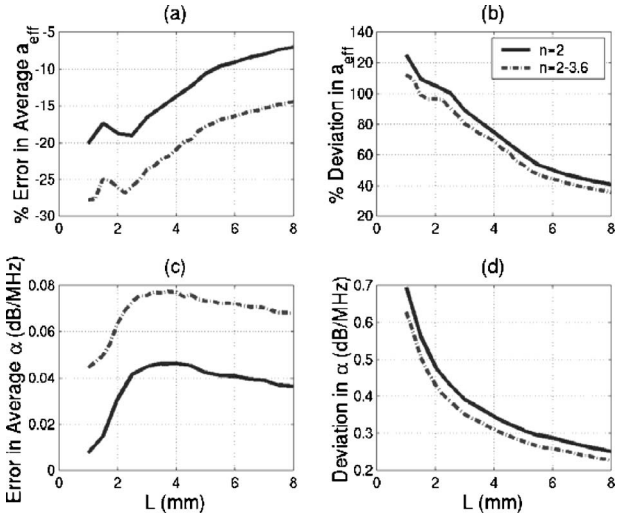

FIG. 9. A comparison between the basic SPECTRAL FIT algorithm ($n=2$) and varying the assumed form factor ($n=2-3.6$) and then extrapolating to find the final estimate for (a) the percent error in the average scatterer size, (b) the percent deviation in the scatterer size, (c) the error in the average total attenuation, and (d) the deviation in the total attenuation for different window lengths.

precision, however, the filtering consistently degrades the performance. The ratio in Fig. 7(b) is always greater than one while the ratio in Fig. 7(c) is greater than or approximately equal to one. Because it is the precision of the estimates that serves as the limiting factor of the SF algorithm, and not the accuracy, using homomorphic deconvolution to smooth each spectrum before averaging provides no benefit to the algorithm when there are 40 wave forms per set.

Although filtering does not provide any benefit when there are 40 wave forms per set, some improvement may occur when there are fewer wave forms available for averaging in the spectral domain. Hence, the simulations were re-evaluated for a Hamming window length of 3 mm with the wave forms grouped into independent sets of 2, 5, 10, and 25 wave forms. For the sake of comparison, a total of 50 estimates were made for each of the different wave form groupings. Hence, not all 2000 of the previously generated wave forms were needed. Figure 8 shows the precision results for each grouping of the wave forms where the upper and lower σ values from Eq. (12) are plotted above and below the axis, respectively. The first bar in each group corresponds to the case where no homomorphic filtering was applied to the wave forms while the second, third, fourth, and fifth bars correspond to results for filter lengths of 0.15, 0.31, 0.46, and 0.62 μs, respectively.

A systematic improvement in precision occurs as the number of independent wave forms used to obtain the estimate is increased (Fig. 8). However, for a given number of wave forms in a set, there is no improvement in precision provided by homomorphic deconvolution. The only possible exception occurs when there are only two wave forms per set, but the overall precision for this case is so poor that the amount of improvement is insignificant. Hence, homomorphic deconvolution does not allow for fewer wave forms to be used in the estimation scheme for the same level of precision.

From this investigation, homomorphic deconvolution clearly does not provide a benefit to the SF algorithm. The poor precision of the SF algorithm is probably related to the slowly varying spectral fluctuations (i.e., small τ_{cep} values) rather than the fast spectral fluctuations that were effectively removed by processing the signals in the cepstral domain. Hence, future algorithms should not be concerned about smoothing the spectra, but rather the emphasis should be placed on reducing the impact of gradual changes to the spectra resulting from the random scatterer spacing. Unfortunately, removing the smooth perturbations is a much more challenging problem.

B. Varying form factor

Another signal processing strategy investigated to improve the precision of the SF algorithm that did not work involved varying the assumed frequency dependence of the form factor describing the scatterer geometry. The correct form factor when using scatterers with a Gaussian impedance distribution is given by

$$F_\gamma(f,a_{\text{eff}}) = \exp(-0.827 \cdot (ka_{\text{eff}})^n), \tag{26}$$

where $n=2$ (Insana *et al.*, 1990). Different estimates for scatterer size and total attenuation can be found by varying the value of n and solving the minimization routine of the SF algorithm for each value of n. A final estimate is then obtained by fitting a line to the estimates versus n values and extrapolating the scatterer size for an n value of 2. In the fit, the n values were weighted by 1 over the minimum value of ASD from Eq. (4). Hence, the estimates corresponding to the better fits from the minimization routine would have a larger impact on the final estimate.

Some simulation results using varying form factors are presented in Fig. 9 along with the results for the basic SF algorithm. These results were obtained using a half-space with an attenuation of 0.3 dB/cm MHz containing Gaussian scatterers with effective radii of 25 μm while varying the

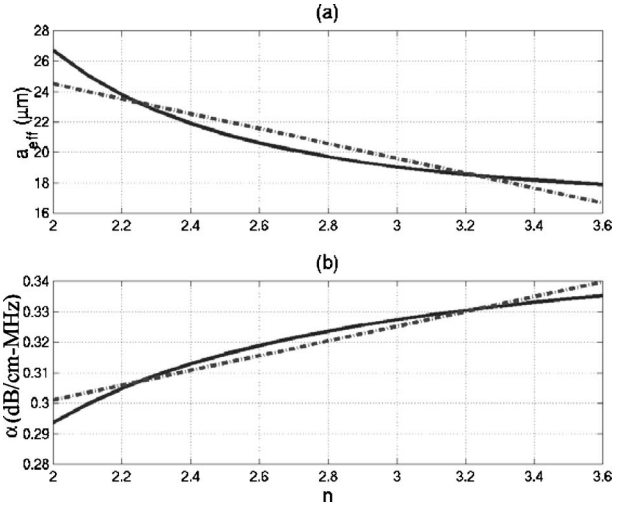

FIG. 10. Example scatterer size and total attenuation estimates at each value of the assumed form factor (solid line) along with the corresponding extrapolation line (dashed line).

assumed value of n from 2 to 3.6 in steps of 0.1. Smaller values of n (i.e., less than 2) were also considered, but the results were not qualitatively different from the ones shown. Once again, 1000 wave forms were generated corresponding to 1000 independent scatterer distributions. The wave forms were grouped into sets of 25 (yielding 40 final estimates), windowed with Hamming windows, and averaged in the normal spectral domain. The convolution impact of windowing was compensated. The percent deviation was also found by adding the upper and lower σ values from Eqs. (12) and (13). Varying the frequency dependence of the form factor from 2 to 3.6 provides an insignificant amount of improvement to the precision of the estimates [Figs. 9(b) and 9(d)] while degrading the accuracy of the estimates [Figs. 9(a) and 9(c)] by about 8%.

The lack of improvement can be understood by considering the results for each assumed form factor along with the linear fit for an example spectrum shown in Fig. 10. A Hamming window with a length of 3 mm was used to obtain these results. The curve is smooth. Hence, variations in the assumed frequency dependence of the form factor do not produce statistically independent estimates and as a result did not improve the precision of the estimation scheme.

The curves shown in Fig. 10 also demonstrate that if the correct form factor (i.e., scatterer geometry) was not known, then reasonable estimates for the total attenuation would still be obtainable. For example, if a frequency dependence of 2.25 is selected (similar to the frequency dependence of a spherical shell type scatterer over some frequency bandwidths), then the estimated attenuation value would differ by only about 0.01 dB/cm MHz from the value given for the true frequency dependence of 2. Unfortunately, the scatterer size will still vary with the form factor because the constant term (i.e., 0.827 for Gaussian scatterers) will vary depending upon the scatterer geometry. However, applications that only require the *in vivo* incident power spectrum, obtainable from the total attenuation, and not the scatterer size, would still benefit from the estimation scheme based on these results even when the correct form factor is not known. This conclusion is important because the correct form factor for biological tissue remains to be determined.

In order to further validate these results, an experiment was performed using a glass-bead phantom (i.e., Gaussian form factor does not apply). The radius of the glass beads in the phantom varied from 22.5 to 26.5 μm and the beads were placed at a density of approximately 48/mm^3 (Madsen *et al.*, 1999). The phantom had an attenuation of 0.826 ± 0.1 dB/cm MHz as measured in our lab monitoring the decay in the backscatter with distance as well as insertion loss measurements. A single-element f/4 spherically focused transducer (Valpey Fisher Instruments, Inc., Hopkinton, MA) with a focal length of 5.54 cm was used to obtain the backscattered signals. The transducer was shock excited by a Panametrics 5900 (Waltham, MA) pulser/receiver operating in pulse/echo mode. $H(f)$ for the transducer followed a Rayleigh function similar to the form given in Eq. (9) and was given by

$$|H(f)| = \frac{|f| \exp\left(-\left(\frac{f - 6.86\ \text{MHz}}{9.04\ \text{MHz}}\right)^2\right)}{\max_{\forall f}\left(|f| \exp\left(-\left(\frac{f - 6.86\ \text{MHz}}{9.04\ \text{MHz}}\right)^2\right)\right)}. \quad (27)$$

In the experiment, the focus of the transducer was positioned 15 mm into the phantom and 875 independent wave forms were acquired using a microprecision positioning system (Daedal Inc., Harrison City, PA) where each wave form was separated by ~ 1 beamwidth. Each wave form was averaged 1000 times to remove noise by a digital oscilloscope (LeCroy 9354 TM, Chestnut Ridge, NY) using a sampling frequency of 100 MHz before being transferred to a computer for later processing. As a result, the noise floor for the experiment was around -30 dB. The averaged independent wave forms were then windowed by a Hamming window with a length of 3 mm [corrected for windowing using Eq. (17)], grouped into sets of 25, and averaged in the normal frequency domain to obtain 35 measurements of $P_{\text{scat}}(f)$. The values of P_{scat} were corrected for the mylar sheet boundary of the phantom so that the attenuation results could be directly compared to earlier experimental results of the phantom's attenuation. The -20 dB bandwidth of the P_{scat} signals was then used in the SF algorithm along with a P_{ref} obtained from the reflection returned by a smooth Plexiglas™ plane placed at the focal plane to obtain 35 estimates of scatterer size and total attenuation.

In the earlier implementations of the SF algorithm involving simulated Gaussian scatterers, a simple minimization routine could be utilized because the ASD surface given by Eq. (4) only had one clearly defined minimum. In the phantom experiment, the ASD surface could have multiple minima with one minimum being significantly lower in value than the others. In this work, the problem of multiple minima was avoided by mapping out the entire ASD surface over a range of possible scatterer sizes and attenuation values, and then, finding the scatterer size and attenuation value that gave the global minimum. The ASD surface was determined for scatterer sizes from 0 μm to two times the scatterer size

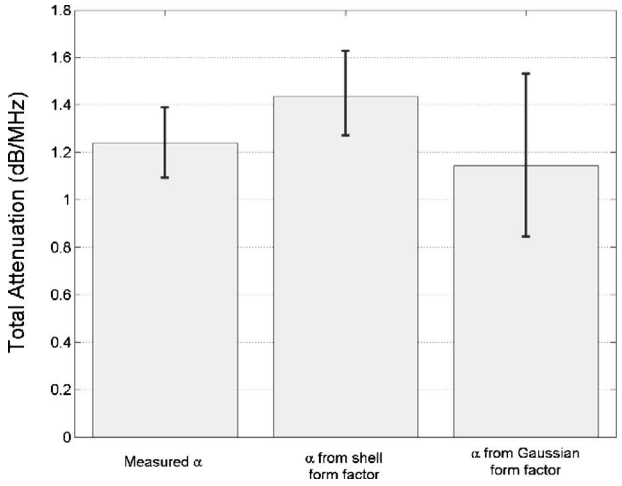

FIG. 11. Comparison of the measured total attenuation for the phantom to the total attenuation found using the SPECTRAL FIT algorithm assuming a spherical shell form factor and a Gaussian form factor.

found when using the traditional size-estimation scheme (Insana *et al.*, 1990) where the attenuation was known (i.e., measured phantom attenuation). The range of attenuation values for the ASD surface was then determined by finding the attenuation value that minimized the ASD when the scatterer size was set at 0 μm and two times the scatterer size from the traditional estimation scheme, respectively.

In order to show the independence of the attenuation estimate on the exact form factor, the analysis using the SF algorithm was performed twice. First, the glass-bead scatterers were described using the correct spherical shell form factor [i.e., $F_\gamma(f,a_{\text{eff}})=(\text{sinc}(2ka_{\text{eff}}/\pi))^2$] (Insana *et al.*, 1990). Using the correct form factor, the mean value for the scatterer radius was 22.5 μm, $\sigma_{a_{\text{upper}}}$ was 2.2 μm, and $\sigma_{a_{\text{lower}}}$ was 3.7 μm which is in the range of the actual sizes of the glass beads. Then, the analysis was repeated using a Gaussian form factor [i.e., $F_\gamma(f,a_{\text{eff}})=\exp(-0.827\cdot(ka_{\text{eff}})^2)$]. Using the Gaussian form factor, the mean value for the scatterer effective radius was 40.0 μm, $\sigma_{a_{\text{upper}}}$ was 7.3 μm, and $\sigma_{a_{\text{lower}}}$ was 10.4 μm. The total attenuation results for both form factors are shown with the measured attenuation results for the phantom in Fig. 11. The mean values for the total attenuation using both form factors are within 0.2 dB/MHz of the average measured value. Hence, knowing the exact form factor is not critical when estimating attenuation along the propagation path however, it is critical when estimating the scatterer size.

IV. CONCLUSION

Six signal processing strategies were evaluated. The best precision was obtained when averaging rf spectra in the normal frequency domain rather than the log domain. The convolution effects of windowing were reduced by approximating the windowing function as a Gaussian transformation on an ideal backscattered Gaussian spectrum. Although the use of Gaussian approximations when solving for the scatterer size and total attenuation had previously been shown to be invalid (Bigelow *et al.*, 2005), a Gaussian approximation of the backscattered spectrum was sufficiently valid to correct for the effects of windowing. After investigating the windowing correction, an improved method for selecting the frequency range used in the minimization for the SF algorithm was discussed. Also, the correction for electronic noise introduced in Bigelow *et al.* (2005) was improved by oversampling the backscattered rf wave form and using the information at higher frequencies to estimate the noise level, thus removing the need to acquire a reference noise signal in the absence of a transmitted signal.

Two approaches were also presented that improved our understanding of the problem. First, homomorphic deconvolution removed the rapid spectral fluctuations from the averaged backscattered power spectrum. The homomorphic-processed signals had no improvement over the basic SF algorithm. The rapid fluctuations on the spectrum are probably not important when solving for the scatterer size and total attenuation using the SF algorithm. Instead, the gradual frequency dependencies resulting from the random scatterer spacing probably corrupt the estimates from the SF algorithm leading to the poor precision.

The second signal processing strategy that failed to improve the precision of the SF algorithm involved varying the assumed form factor and then extrapolating to obtain size and attenuation estimates at the correct value of the form factor. The extrapolated values had poorer accuracy and the same precision as directly estimating the size and attenuation using the correct form factor. It was observed that the estimate for total attenuation had only a weak dependence on the form factor. This conclusion was further validated using a phantom experiment. As a result, the SF algorithm should yield accurate estimates of total attenuation when the correct form factor is not known.

ACKNOWLEDGMENTS

This work was supported by the University of Illinois Research Board, by a NDSEG Fellowship awarded to T.A.B., and by a Beckman Institute Graduate Fellowship awarded to T.A.B.

Akita, M., and Ueda, M. (**1988**). "The effects of windowing on spectral estimation of echoes scattered by a random medium," J. Acoust. Soc. Am. **107**, 1243–1248.

Bigelow, T. A. (**2004**). "Estimating the medical ultrasound *in vivo* power spectrum," Ph.D. dissertation, University of Illinois at Urbana-Champaign.

Bigelow, T. A., and O'Brien, W. D., Jr. (**2004**). "Scatterer size estimation in pulse-echo ultrasound using focused sources: Theoretical approximations and simulation analysis," J. Acoust. Soc. Am. **116**, 578–593.

Bigelow, T. A., Oelze, M. L., and O'Brien, W. D., Jr. (**2005**). "Estimation of total attenuation and scatterer size from backscattered ultrasound waveforms," J. Acoust. Soc. Am. **117**, 1431–1439.

Gerig, A., Zagzebski, J., and Varghese, T. (**2003**). "Statistics of ultrasonic scatterer size estimation with a reference phantom," J. Acoust. Soc. Am. **113**, 3430–3437.

Insana, M. F., Wagner, R. F., Brown, D. G., and Hall, T. J. (**1990**). "Describing small-scale structure in random media using pulse-echo ultrasound," J. Acoust. Soc. Am. **87**, 179–192.

Lee, D. J., Sigel, B., Swami, V. K., Justin, J. R., Gahtan, V., O'Brien, S. P., Dwyer-Joyce, L., Feleppa, E. J., Roberts, A. B., and Berkowitz, H. D. (**1998**). "Determination of carotid plaque risk by ultrasonic tissue characterization," Ultrasound Med. Biol. **24**, 1291–1299.

Lizzi, F. L., Astor, M., Liu, T., Cheri, D., Coleman, D. J., and Silverman, R. H. (**1997a**). "Ultrasonic spectrum analysis for tissue assays and therapy evaluation," Int. J. Imaging Syst. Technol. **8**, 3–10.

Lizzi, F. L., Greenebaum, M., Feleppa, E. J., and Elbaum, M. (**1983**). "The-

oretical framework for spectrum analysis in ultrasonic tissue characterization," J. Acoust. Soc. Am. **73**, 1366–1373.
Lizzi, F. L., Kalisz, A., Astor, M., Coleman, D. J., Silverman, R. H., and Reinstein, D. Z. (**1997b**). "Very-high frequency ultrasonic imaging and spectral assays of the eye," Acoust. Imaging **23**, 107–112.
Lizzi, F. L., Muratore, R., Deng, C. X., Ketterling, J. A., Alam, K. A., Mikaelian, S., and Kalisz, A. (**2003**). "Radiation-force technique to monitor lesions during ultrasonic therapy," Ultrasound Med. Biol. **29**, 1593–1605.
Lizzi, F. L., Ostromogilsky, M., Feleppa, E. J., Rorke, M. C., and Yaremko, M. M. (**1986**). "Relationship of ultrasonic spectral parameters to features of tissue microstructure," IEEE Trans. Ultrason. Ferroelectr. Freq. Control **33**, 319–329.
Lu, Z. F., Zagzebski, J. A., and Lee, F. T. (**1999**). "Ultrasound backscatter and attenuation in human liver with diffuse disease," Ultrasound Med. Biol. **25**, 1047–1054.
Madsen, E. L., Dong, F., Frank, G. R., Garra, B. S., Wear, K. A., Wilson, T., Zagzebski, J. A., Miller, H. L., Kirk, Shung K., Wang, S. H., Feleppa, E. J., Liu, T., O'Brien, W. D., Jr., Topp, K. A., Sanghvi, N. T., Zaitsev, A. V., Hall, T. J., Fowlkes, J. B., Kripfgans, O. D., and Miller, J. G. (**1999**). "Interlaboratory comparison of ultrasonic backscatter, attenuation, and speed measurements," J. Acoust. Soc. Am. **18**, 615–631.
Nightingale, K. L., Nightingale, R. W., Palmer, M. L., and Trahey, G. E. (**2000**). "A finite element model of remote palpation of breast lesions using radiation force: Factors affecting tissue displacement," Ultrason. Imaging **22**, 35–54.
Noritomi, T., Sigel, B., Swami, V., Justin, J., Gahtan, V., Chen, X., Feleppa, E. J., Roberts, A. B., and Shirouzu, K. (**1997**). "Carotid plaque typing by multipile-parameter ultrasonic tissue characterization," Ultrasound Med. Biol. **23**, 643–650.
O'Donnell, M., Skovoroda, A. R., Shapo, B. M., and Emelianov, S. Y. (**1994**). "Internal displacement and strain imaging using ultrasonic speckle tracking," IEEE Trans. Ultrason. Ferroelectr. Freq. Control **41**, 314–325.
Oelze, M. L., O'Brien, W. D. Jr., Blue, J. P., and Zachary, J. F. (**2004**). "Differentiation and characterization of rat mammary fibroadenomas and 4T1 mouse carcinomas using quantitative ultrasound imaging," IEEE Trans. Med. Imaging **23**, 764–771.
Ophir, J., Céspedes, I., Ponnekanti, H., Yazdi, Y., and Li, X. (**1991**). "Elastography: A quantitative method for imaging the elasticity of biological tissues," Ultrason. Imaging **13**, 111–134.
Proakis, J. G., and Manolakis, D. G. (**1996**). "*Digital Signal Processing: Principles, Algorithms, and Applications*," 3rd ed. (Prentice Hall, Upper Saddle River, NJ), Chap. 4, pp. 365–367.
Silverman, R. H., Folberg, R., Rondeau, M. J., Boldt, H. C., Lloyd, H. O., Chen, X., Lizzi, F. L., Weingeist, T. A., and Coleman, D. J. (**2003**). "Spectral parameter imaging for detection of prognostically significant histological features in uveal melanoma," Ultrasound Med. Biol. **29**, 951–959.
Skovoroda, A. R., Emelianov, S. Y., Lubinski, M. A., Sarvazyan, A. P., and O'Donnell, M. (**1994**). "Theoretical analysis and verification of ultrasound displacement and strain imaging," IEEE Trans. Ultrason. Ferroelectr. Freq. Control **41**, 302–313.
Skovoroda, A. R., Emelianov, S. Y., and O'Donnell, M. (**1995**). "Tissue elasticity reconstruction based on ultrasonic displacement and strain images," IEEE Trans. Ultrason. Ferroelectr. Freq. Control **42**, 747–765.
Wear, K. A. (**2001**). "Fundamental precision limitations for measurements of frequency dependence of backscatter: Applications in tissue mimicking phantoms and trabecular bone," J. Acoust. Soc. Am. **110**, 3275–3282.
Wear, K. A. (**2002**). "A Gaussian framework for modeling effects of frequency-dependent attenuation, frequency-dependent scattering, and gating," IEEE Trans. Ultrason. Ferroelectr. Freq. Control **49**, 1572–1582.